 doi:10.20944/preprints202206.0095.v1

Article

Optimization of Mechanosensitive Cross-talk between Matrix Stiffness and Protein Density: Independent Matrix Properties Regulate Spreading Dynamics of Myocytes

Judith Brock [1], Julia Erhardt [1], Stephan A. Eisler [2] and Marcel Hörning [1,*]

[1] Biobased Materials Laboratory, Institute of Biomaterials and Biomolecular Systems, University of Stuttgart, 70569 Stuttgart, Germany
[2] Stuttgart Research Center Systems Biology (SRCSB), University of Stuttgart, 70569 Stuttgart, Germany
* Correspondence: marcel.hoerning@bio.uni-stuttgart.de

Abstract: Cells actively sense differences in topology, matrix elasticity and protein composition of the extracellular microenvironment and adapt their function and morphology. In this study, we focus on the cross-talk between matrix stiffness and protein coating density that regulate morphology and proliferation dynamics of single myocytes. For this, C2C12 myocytes were monitored on L-DOPA functionalized hydrogels of 22 different elasticity and fibronectin density compositions. Static images were recorded and statistically analyzed to determine morphological differences and to identify the optimized extracellular matrix (ECM). Using that information, selected ECMs were used to study the dynamics before and after cell proliferation by statistical comparison of distinct cell states. We observed a fibronectin density independent increase of the projected cell area until 12 kPa. Additionally, changes in the fibronectin density led to an area optimum at about 2.6 $\mu g/cm^2$, which was confirmed by an independent F-actin analysis, revealing a maximum actin filament to cell area ratio of 7.5 %. The proliferation evaluation showed an opposite correlation between cell spreading duration and speed to the matrix elasticity and protein density, which did not affect the cell cycle duration. In summary, we identified an optimized ECM composition, while independent matrix properties regulate distinct cell characteristics.

Keywords: mechanosensitivity, proliferation, myocyte, actincytoskeleton, extracellular matrix, L-DOPA

1. Introduction

Forces in biology can act on various scales, ranging from entire muscle actuation of larger mammalians down to single sub-cellular actin contractions of individual cells. While muscles are controlled by the nervous system, single cells self-regulate and respond to the extracellular matrix (ECM) through mechanosensitive properties[1]. There are many external cues that enable cells to actively react to the extracellular microenvironment through different signaling pathways. External passive properties of the ECM, i.e. elasticity[2,3] and topology[4,5], are sensed through focal adhesion complexes[6] and can lead to changes in cell morphology and regulative signaling. The latter are large macromolecular assemblies distributed at the plasma membrane of cells that can trigger mechanical force generation via actin-myosin complexes[7]. Variable environmental signals, i.e. galvanotaxis, phototaxis and chemotaxis, can also lead to an activation of intracellular force generation. Heart cells, for example, may generate a signaling cascade (membrane potential) to induce cell contraction through an initial increase of the sodium concentration through connective gap-junction of adjacent cells[8]. During development and starvation, *Dicytostelum discoideum* cells sense the excretion of extracellular cAMP and light, in order to form multicellular structures[9]. Chemical gradients play also an important role during embryogenesis and morphogenesis in many other species, such as in Drosophila[10], mouse[11], and even plants[12].

 doi:10.20944/preprints202206.0095.v1

As cells have the ability to sense and react to the ECM, it is crucial to provide an optimal mechanical, topological and molecular environment in artificial culture systems. Here, the term 'optimal' refers to the natural environment, as cells have developed to fulfill a specific function, which is predetermined by the developmental lineage of a specific environment[13]. Specific examples are the optimal matrix stiffness of about 12 kPa that mimics muscle tissue elasticity, leading to optimized myotube differentiation[14], cardiac wave beat[15] and synchronization dynamics[2], as well as actomyosin stress-fibre alignment[16]. On the other hand, the optimal matrix protein density (collagen, 0.1 - 1.0 µg/mL) of the ECM leads to an increased spread of smooth muscle cells[17], while different cell types and matrix proteins may exhibit very different optimal conditions, such as epithelial cells cultured with fibronectin at 0.05 µg/mL[18].

During the last decade, many advanced methods have been developed to study the influence of dynamical ECM changes to cells, such as dynamically tuneable hydrogels [3,19], three-dimensional scaffolds [4,20], and even the 3D-printed cell scaffolds that mimic native tissue composition and mechanics [5]. However, the influence and cross-talk between matrix stiffness and protein density has not been studied very conclusively and systematically yet. In this study, we focus on the morphology and proliferation dynamics of single C2C12 muscle cells on rigid acrylamide-based hydrogels that are functionalized with distinct fibronectin densities. By statistical analysis of an extended number of cells, we first reproduced the well established relationship between projected cell area and substrate rigidity, as shown before for various cell types, e.g. C2C12 [3,14,19], embryonic cardiomyocytes [15], mesenchymal stem cells[13], and epidermal stem cells [21]. We identified a transition from smaller to larger projected cell areas independent of the fibronectin density at about 12 kPa. Next, we fixed the substrate rigidity and varied the fibronectin densities revealing an optimal fibronectin density at about 2.6 µg/cm^2, where cells exhibit not only the largest cell areas but also an optimally situated actin-cytoskeleton. Based on these findings, we statistically investigated the proliferation dynamics of cells through the parameterisation of distinct morphological cell states before and after cell division. Most interestingly, we found that the spreading speed of the cell area depends on the fibronectin density, while the duration of spreading after the cell division depends solely on the matrix rigidity. Although cells displayed distinct mechano-regulative dynamics that depend on the ECM composition, they did not show changes in the cell cycle duration.

2. Materials and Methods

Glass preparation.

Glass substrates (22mm, Δh = 0.12 - 0.17 mm, Matsunami, C022001) and cover glasses (24 × 24 mm^2, VWR, ECN631-1571) were cleaned using a modified RCA method[3,22] according to the following procedures. The glasses were (1) subsequently rinsed and sonicated in acetone, ethanol, methanol and distilled water for 3 min; (2) immersed in hydrogen peroxide solution ($H_2O : H_2O_2 : NH_3$ aq. as 5:1:1), sonicated for 3 min and kept at 60°C for 30 min; (3) rinsed 10 times with distilled water; (4) and finally oven-dried at 70°C for at least 3 hours. Vinyl-silanized glass substrates were prepared to chemically fix the hydrogels. The RCA-cleaned round glass substrates were immersed in 5 % (v/v) vinyltrimethoxysilane in toulene (Sigma-Aldrich, 235768) and shaken for 18 h at room temperature. Thereafter the hydrogels were sequentially rinsed with acetone, ethanol and distilled water, and dried at 140°C for 1 hour[23].

Hydrogel preparation.

Poly-acrylamide hydrogels were prepared by fixing the cross-linker ratio to 2% combining a 40 % acrylamide (AAm, Carl Roth, 7748.1) and 2 % bis-acrylamide solution (bAAm, Carl Roth, 3039.2) in water. The molarity of the hydrogels was varied between 0.6 mol · kg^{-1} and 2.0 mol · kg^{-1}. A stock solution of about 1 mL was freshly prepared (Tab. 1) of which 200 µL were combined with 10% ammonium peroxodisulfate (4.6 µL,

Preprints (www.preprints.org) | NOT PEER-REVIEWED | Posted: 7 June 2022 doi:10.20944/preprints202206.0095.v1

APS, Sigma, A3678) and N,N,N′,N′- tetramethylethylenediamine (0.3 µL, TEMED, Carl Roth, 2367.3). For each hydrogel, a 20 μL portion of the mixed solution was sandwiched between a round vinyl-silanized glass substrate and a square-shaped cover glass and kept for 30 min at RT[24]. After removing the cover glass, the hydrogel was successively soaked in water for at least 48 hours to remove the residual chemicals.

Table 1. Hydrogel preparation.

total monomer concentration, C_m [mol·kg^{-1}]	**H_2O [µL]**	**AAm [µL]**	**bAAm [µL]**
0.60	780.2	104.5	92.5
0.80	714.5	139.3	123.3
1.00	648.9	174.2	154.2
1.25	566.8	217.7	192.7
1.50	484.7	261.2	231.3
1.75	402.6	304.8	269.8
2.00	320.6	348.3	308.3

Mechanical testing.

The Young's modulus E of the hydrogels was measured by nanoindentation using an atomic force microscope (NanoWizard, JPK Instruments, Berlin). The hydrogels were indented by a spherical colloidal probe that was attached to a silicon-nitride cantilever with a nominal spring constant of 0.08 N/m (CP-PNP-BSG; R = 5 μm, Olympus Optical) and an approaching speed of 1 μm/s. Each cantilever was calibrated and the spring constant was determined by the thermal noise measurement[25]. The measured force-indentation curves were analyzed by nonlinear least-squares fitting to the Hertz model [22,26,27] using a customized Matlab (Mathworks) routine. The modified Hertz model equation for spherical indenter-shapes to determine E was fitted as

$$F = 4ER^{1/2} \cdot [3(1-\nu)^2]^{-1} \cdot \delta^{3/2}, \quad (1)$$

where F is the force applied to the indenter, $\nu = 0.5$ the Poisson's ratio, and δ is the indentation depth[3,28]. The average Young's modulus of 50 independent indentation-sites at two 100 × 100 μm^2 areas was quantified for each hydrogel to ensure statistical significance.

Height determination.

The height of the hydrogels was measured by autofluorescence signal observation using a Laser Scanning Microscope (LSM 710, Carl Zeiss Microscopy GmbH, Jena, Germany) equipped with a X40 magnification objective lens (Plan-Neofluar 40x/1.3 DIC numerical aperture 0.60; Carl Zeiss Microscopy GmbH, Jena, Germany). The following setting was used: 75% laser intensity, 488 nm excitation wavelength, 509 nm to 740 nm emission bandwidth, a pinhole of 40, and a gain of 1015. The serial images were recorded with a spatial resolution of $\Delta x = \Delta y = 2.768$ µm (128 × 128 pixels, 8 bit) and $\Delta z = 1.0$ µm. For every molarity at least two hydrogels with five positions were measured. The average intensity signal of each image was calculated and normalized to determine the hydrogel height. The height was obtained by measuring the distance between the autofluorescence intensity peaks at the glass to gel and gel to medium interface. All data were analyzed with custom routines in Matlab (R2018b; The MathWorks, Natick, MA).

Surface functionalization.

For functionalizing the surface of the hydrogels the catecholamine L-DOPA (3,4-Dihydroxy-L-phenylalanin, Sigma-Aldrich; D9628) was used. L-DOPA was dissolved in freshly prepared TRIS buffer (10 mM, pH 10, Roth 4855.2) at a final concentration of

Preprints (www.preprints.org) | NOT PEER-REVIEWED | Posted: 7 June 2022 doi:10.20944/preprints202206.0095.v1

2 mg/mL for 30 min in dark on a tube roller, and sterilized through a 0.2 µm filter (Filtropur S0.2, Sarstedt 83.1826.001)[29]. The hydrogels were washed with TRIS buffer and 250 µL of the L-DOPA solution were added on each hydrogel. After 30 min of incubation in the dark (RT) the samples were washed two times with PBS to remove unbound L-DOPA. On the functionalized hydrogel fibronectin (FN) from human plasma (Sigma, F2006), prepared with PBS, was applied at the desired concentration (Table 2), and allowed to react for at least 2 hours at 37 °C [3,30]. Prior to cell seeding, the hydrogels were washed with cell culture medium to remove unbound excess of fibronectin.

Table 2. Protocol for fibronectin coating densities.

FN coating density, ρ_{FN} [**µg**/cm^2]	**volume on gel** [µL]	**FN concentration** [mg/mL]
0.4	300	5.00
1.1	250	16.72
1.8	250	27.36
2.6	250	40.00
3.3	250	50.16
4.0	250	60.80

Cell Culture

Mouse myoblast cells (C2C12, <30 passages, Sigma-Aldrich) were cultured in Dulbecco's modified Eagle's medium (DMEM, D6046, Sigma-Aldrich) supplemented with 10 % fetal bovine serum (F9665, Sigma-Aldrich), and 1% penicillin-streptomycin (P0781, Sigma-Aldrich). The cells were enzymatically digested using Trypsin-EDTA solution (0.25%, T4049, Sigma) to detach them from the culture flask. Thereafter the cells were counted and seeded depending on the substrate properties with a cell-density between 5 cells/mm^2 and 70 cells/mm^2 on the fibronectin-coated substrates 24 hours before the observation (F2006, Sigma-Aldrich). The cells were maintained in a humidified incubator at 37°C and 5% CO_2.

Image and time-lapse acquisition

Phase-contrast images were obtained by using an inverted microscope (Axiovert 200M; Zeiss, Carl Zeiss Microscopy GmbH, Jena, Germany) through a X20 magnification objective lens (LD ACHROPLAN 20x/0.40; Carl Zeiss Microscopy GmbH, Jena, Germany) and a CCD Camera (Zeiss AxioCam MRm) at a resolution of $\Delta x = \Delta y = 0.322$ µm (Axiovision, Ver. 4.8). The time-lapse recorded phase contrast images were obtained by using an inverted microscope (Zeiss Cell Observer Z1; Carl Zeiss Microscopy GmbH, Jena, Germany) through a X40 magnification objective lens (Plan-Neofluar 40x/0.6 Korr Ph2, Carl Zeiss Microscopy GmbH, Jena, Germany) and a CCD Camera (Zeiss AxioCam 503 mono) at a resolution of $\Delta x = \Delta y = 0.332$ µm after 2 × 2 binning under physiological humidified conditions (37°C, 5% CO_2).

Fluorescence staining

The cells were washed with PBS and fixed with 4% formaldehyde (Promega, 104003) in PBS for 20 minutes at RT and washed three times for 10 minutes in PBST (0.1% Tween 20, Carl Roth, 9127.1, in PBS). Phalloidin (200 U/mL in Methanol, Alexa fluor 546, Invitrogen, A22283) was added to DAPI (1 µg/mL in PBST) solution (1:800), and 400 µL per sample were incubated in the dark for 1 hour at RT. The samples were washed three times for 10 minutes in PBST and stored in PBS at 4°C until observation on the next day.

LifeAct transfection

The cells were plated on hydrogels with a density of 100 cells/cm^2 and incubated in DMEM for 24 hours before transfection. On day of transfection, cells were washed with PBS and DMEM was changed to antibiotic-free DMEM. For every transfection sample 0.7 µL of

Preprints (www.preprints.org) | NOT PEER-REVIEWED | Posted: 7 June 2022 doi:10.20944/preprints202206.0095.v1

plasmid (pCMV- LifeAct-TagGFP2, ibidi, 60101, 1 µg/µL) and 2.1 µL of Lipofectamine 2000 (Invitrogen, 11668-030) were added to individual microcentrifuge tubes containing 100 µL PBS each. Both tubes were then combined and incubated for 20 min at RT in the dark. The solution of about 200 µL was added dropwise to the cells while shaking the sample carefully. Medium was changed to DMEM containing penicillin-streptomycin 24 hours after transfection and cells were observed for 30 hours.

Image acquisition of fluorescent cells

DAPI- and Phalloidin-stained C2C12 cells were imaged using the AxioObserver SD confocal microscope (Zeiss) equipped with Yokogawa CSU-X1 Spinning Disk Unit using a X40 objective (Plan-Apochromat 1.4 Oil DIC UV, Zeiss) with the Axiocam 503 Mono CCD camera at a resolution of $\Delta x = \Delta y = 0.227$ µm. For the image acquisition and analysis, the ZEN blue 2.3 software was used. For the visualisation of the nuclei and F-Actin, 405 nm (DAPI) and 561 nm (Phalloidin) diode lasers were used. Each image was recorded as a 5×5 tile composition with 5 focal heights ($\Delta z = 1$ µm). Lifeact-tagged C2C12 cells were imaged using the same imaging system (561 nm diode lasers), but with a EMCCD Camera (Photometrix Evolve 512) at a resolution of $\Delta x = \Delta y = 0.333$ µm. Each image was recorded as a 3×3 tile composition with 5 focal heights ($\Delta z = 1$ µm) every $\Delta t = 15$ min. Tiles were stitched using the "fuse tiles" and "correct shading" features of the ZEN 2.3 software followed by creating an orthogonal projection of the maximum intensity merging all recorded Z-stacks.

Actin Quantification Analysis (AQuA)

The actin filaments of C2C12 cells were quantified by actin filament orientation analysis using an algorithm written in Matlab (R2021b; The MathWorks, Natick, MA) [3,5,16,31]. The Laplacian filter

$$\begin{bmatrix} 0 & -1 & 0 \\ -1 & 4 & -1 \\ 0 & -1 & 0 \end{bmatrix} \tag{2}$$

and $n = 15$ differently rotated anisotropic Gaussians with $\sigma_x = 4\sigma_y$ were convoluted to elongated Laplace of Gaussian (eLoG) kernels. The kernels were applied to the original images (tile composition) and the maximum response of each pixel was calculated, as

$$I_{\max}(n, x, y) = \max[\text{eLoG}(n) \times I(x, y)]. \tag{3}$$

Thereafter, $I_{\max}$ was processed by the binarized original images using the Otsu's thresholding method[32]. Connected fibers of the same rotational direction with less than 10 pixels were removed. The obtained actin fibers were colorised with a color scheme that corresponds to the local actin orientation angles, θ_n.

Phalloidin-stained and Lifeact-tagged cells were analysed with $\sigma_x^{\text{Phal}} = 1$ and $\sigma_x^{\text{Life}} = 1.5$, so that $\Delta x/\sigma_x$ is constant and therefore proportionally scaled to the respective camera resolution Δx.

Statistical analysis of fluorescent cells

Actin- and nuclei-stained cells that were recorded and statistically analysed as a 5×5 tile composition. The average cell area $\langle A \rangle$ and the average amount of actin per cell $\langle M \rangle$ was calculated using AQuA, as

$$\langle A \rangle = \sum_{5\times5} A \times n_{\text{nuc}}^{-1}, \tag{4}$$

and

$$\langle M \rangle = \sum_{5\times5} M \times n_{\text{nuc}}^{-1} \tag{5}$$

Preprints (www.preprints.org) | NOT PEER-REVIEWED | Posted: 7 June 2022 doi:10.20944/preprints202206.0095.v1

where n_{nuc} is the number of nuclei per image-composition, and $\langle M \rangle$ was obtained by AQuA. The fraction of actin amount to cell area for each image-composition was calculated, as

$$\langle R \rangle = \langle M \rangle \times \langle A \rangle^{-1}. \tag{6}$$

Statistical analysis of phase-contrast cells

The statistical analysis of the projected cell areas was calculated by a log-transformation, because of the strongly skewed normal distributions, as

$$x^i_{\log} = \log(x^i), \tag{7}$$

the mean $\mu_{\log}$ and standard deviation $\sigma_{\log}$ was calculated, as

$$\mu_{\log} = \frac{1}{N}\sum_{i=1}^{N} x^i_{\log} \tag{8}$$

$$\sigma_{\log} = \sqrt{\frac{1}{N}\sum_{i=1}^{N}\left(x^i_{\log} - \mu_{\log}\right)^2}. \tag{9}$$

and back-transformed to obtain the mean and variance in the normal space as

$$\mu = e^{\mu_{\log} + \sigma^2_{\log}/2} \tag{10}$$

$$\sigma^2 = \mu^2\left(e^{\sigma^2_{\log}} - 1\right). \tag{11}$$

following the Finney estimator approach [33], where N is the number of cells. Based on that the standard error with a 95% confidence interval is defined as

$$SE = \frac{2\sigma}{\sqrt{N}}. \tag{12}$$

As an alternative approach the projected cell area distribution was quantified as a mixture of two normal probability density functions (MN-pdf), which is defined by the fractional sum of two normal probability density functions, as

$$P_\Sigma(x|p,\mu_{1,2},\sigma_{1,2}) = p \cdot P(x|\mu_1,\sigma_1) + (1-p) \cdot P(x|\mu_2,\sigma_2), \tag{13}$$

with

$$P(x|\mu,\sigma) = \frac{1}{\sigma\sqrt{2\pi}} \exp\left(\frac{-(x-\mu)^2}{2\sigma^2}\right), \tag{14}$$

where p is the fractional parameter defined between zero and one. The means $\mu_{1,2}$ and the respective standard error of the MN-pdf with a 95% confidence interval are defined as

$$SE_1 = \frac{2\sigma_1}{\sqrt{pN}} \quad \text{and} \quad SE_2 = \frac{2\sigma_2}{\sqrt{(1-p)N}}, \tag{15}$$

where N is the number of cells observed at a certain culture condition.

3. Results

Cell proliferation is a fundamental process for organismal development and homeostasis to ensure complete and precise cell duplication [34]. C2C12 myocytes follow a proliferation-cycle of about 24 hours when grown in a crowded environment. Figure 1 shows a typical example of a C2C12 cell that undergoes proliferation. The actin cytoskeleton is shown to highlight the dynamics and sudden transition from the strongly adhered cell ($t = -15$ min) to the actin depolymerized rounded up cell just before the cell division ($t = 0$ min). Thereafter, the two daughter cells start to spread by increasing their actin poly-

Preprints (www.preprints.org) | NOT PEER-REVIEWED | Posted: 7 June 2022 doi:10.20944/preprints202206.0095.v1

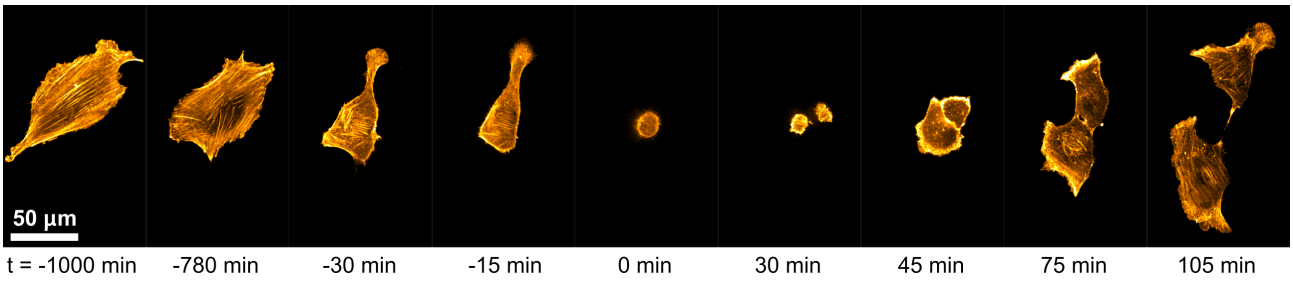

Figure 1. Proliferation dynamic of a single myocyte. Shown is an actin-tagged C2C12 muscle cell on glass that undergoes proliferation at about $t = 0$ min. The two daughter cells increase their size and eventually migrate independently ($t \geq 30$ min).

merization activity. Once the cells overcome a critical size, they start to migrate again. This fundamental cell dynamic repeats and defines a cell cycle. The influence of the extracellular matrix composition, i.e. substrate rigidity and protein density, is crucial for the cellular integrity of the cell cycle, as different mechanical stresses act on the cells and change their response. In this work, we statistically quantify dependencies and differences of the cellular response of single C2C12 on functionalized hydrogels.

Poly-acrylamide hydrogels were prepared as cell culture substrates to study the dynamical changes in the cell-morphology during cell growth and proliferation of single spatially isolated C2C12 myocytes. The chemical composition of the hydrogel was adapted, i.e. total monomer concentration, C_m and cross-linker ratio, so that a single parametric dependence is sufficient to modulate E. Increases in C_m lead to a monotonic decrease in the polymeric network mesh size at a fixed cross-linker ratio[35,36]. Contrarily, changes in the cross-linker ratio lead to non-monotonic changes in E when fixing C_m[37] (see also Fig. S1A), which may have additional effects on the cell viability and dynamics[38]. Figure 2 illustrates the mechanical characterization of the prepared hydrogels. The increase in C_m from 0.6 to 2.0 mol·kg^{-1}, by fixing the cross-linker ratio to 2%, lead to a linear increase in E of about 3 to 35 kPa, respectively (Fig. 2A, Tab. 3). This covers the biologically relevant elasticities in the microenvironment of C2C12 myocytes[14]. Figure 2B shows three nano-indentation curves for 3.2 kPa, 12.0 kPa and 35.0 kPa exemplarily. Additionally, the hydrogel heights were measured using auto-fluorescence signaling. No dependence of the molarity was observed (Fig. 2C). The average height of the hydrogels was measured

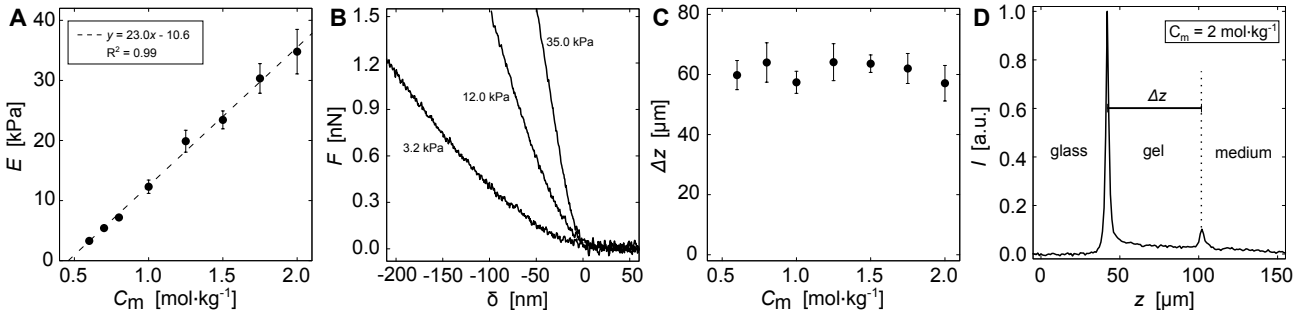

Figure 2. Property assessment of the poly-acrylamide hydrogels. **A** Average Young's modulus E as a function of the total monomer concentration C_m at fixed cross-linker ratio, 2%. The change in C_m shows a linear increase in E, as illustrated by the dashed line. **B** Three nano-indentation curves measured at $C_m = 0.6$, 1.0, and 2.0 mol·kg^{-1}, exemplarily. Shown is the force F as a function of the indentation depth δ. **C** Average height Δz of the hydrogels as a function of C_m, which was obtained by auto-fluorescence measurements using confocal laser scanning microscopy. **D** Example of an auto-fluorescence signal of a hydrogel with C_m = 2.0 mol·kg^{-}1 ($E = 35$ kPa). Shown is the normalized intensity as a function of the height z. The two peaks mark the transitions from glass to gel and gel to culture medium, respectively. The gel height Δz is calculated as the peak to peak distance.

Preprints (www.preprints.org) | NOT PEER-REVIEWED | Posted: 7 June 2022 doi:10.20944/preprints202206.0095.v1

Table 3. Young's modulus of hydrogels measured via AFM and linear fit (see Fig. 2A).

total monomer concentration, C_m **[mol·kg^{-1}]**	**Young's modulus,** E (measured via AFM) **[kPa]**	**Young's modulus,** E (linear fit) **[kPa]**
0.60	3.3 ± 0.2	3.2
0.80	7.2 ± 0.2	7.8
1.00	12.3 ± 1.1	12.4
1.25	19.9 ± 1.8	18.2
1.50	23.4 ± 1.5	23.9
1.75	30.3 ± 2.5	29.7
2.00	34.8 ± 3.7	35.4

to about $\Delta z = 60\,\mu$m, which ensures that the cells cannot sense the underlying glass[24]. Figure 2D shows a typical example of an auto-fluorescence signal measured at a hydrogel with C_m = 2.0 mol·kg^{-1}. The two intensity peaks mark the transitions from glass to gel and gel to culture medium. While the relative height between both peaks can vary, the second peak (gel to medium) can be very shallow. In those cases, the shallow plateau was used to estimate the gel height (Fig. S1B).

Cell-morphological response to substrate properties

The fibronectin functionalized hydrogels were used to characterize the adhesion properties of C2C12 myocytes. A total of 13426 cells with 22 different substrate conditions were observed, consisting of seven different substrate rigidities and six different fibronectin coating densities. Figure 3A illustrates C2C12 myocyte cells cultured on a hydrogel substrate with $E \simeq 12.4$ kPa and $\rho_{\mathrm{FN}} \simeq 2.6\ \mu$g/cm^2. The cells exhibit a broad variation in adhesion area A even when cultured on the same substrate. Figure 3B shows two representative histograms of A for cells cultured on substrates with rigidities $E \simeq 7.8$ kPa and $E \simeq 18.2$ kPa at a constant fibronectin density, $\rho_{\mathrm{FN}} \simeq 2.6\ \mu$g/cm^2. As shown in various studies before [3,14,17,19], an increase in the substrate rigidity leads to an increase in A. A similar tendency is observed when fixing the substrate rigidity ($E \simeq 12.4$ kPa) and variating ρ_{FN}, as plotted for 0.4 μg/cm^2 (blue) and 2.6 μg/cm^2 (orange) (Fig. 3C). An increase in ρ_{FN} leads to an increase in A. The relation between the mean projected cell area $\langle A \rangle$ and the substrate rigidity E for the two fibronectin surface-densities $\rho_{\mathrm{FN}} = 0.4\ \mu$g/cm^2 (blue) and 2.6 μg/cm^2 (orange) is plotted in Fig. 3D. As all distributions are strongly skewed normal distributions, $\langle A \rangle$ was determined by a log-transformation using the Finney estimator approach (see Materials and Methods). The obtained dependencies can be fitted by the empirical Hill equation (dashed lines)

$$\mathcal{H}(E) = \langle A \rangle = \frac{\langle A \rangle_{\max} - \langle A \rangle_{\min}}{(E_{1/2}/E)^m + 1} + \langle A \rangle_{\min}, \tag{16}$$

as demonstrated before [3,13,15], with typical characteristic half levels at $E_{1/2} \simeq 11.8$ kPa and $E_{1/2} \simeq 13.4$ kPa, that represent natural soft muscle tissue. The cooperativity coefficient was arbitrary fixed to $m = 20$, because the data density does not allow a statistically significant estimation of the slopes between the minimum and maximum projected areas, $\langle A \rangle_{\min}$ and $\langle A \rangle_{\max}$. Further, we verified that an increase in fibronectin surface-densities ρ_{FN} leads not only to increased levels of $\langle A \rangle_{\min}$ and $\langle A \rangle_{\max}$ but also to an increase in $E_{1/2}$, considering that $E_{1/2}$ is always at about $E \simeq 12$ kPa. Figure 3E shows $\langle A \rangle$ as a function of ρ_{FN} at the fixed substrate rigidities $E \simeq 12.4$ kPa and $E \simeq 35.4$ kPa. As expected, $\langle A \rangle$ increases for both conditions up to about $\rho_{\mathrm{FN}} \simeq 2\ \mu$g/cm^2. While cells cultured on substrates with $E \simeq 12.4$ kPa exhibits a slightly lower kink at $\rho_{\mathrm{FN}} \simeq 2.6\ \mu$g/cm^2, a maximum $\langle A \rangle$ is observed for $E \simeq 35.4$ kPa. This variation in $\langle A \rangle$ at $\rho_{\mathrm{FN}} \simeq 2.6\ \mu$g/cm^2 can be explained by the sensitive response of cells around $E_{1/2}$. Small changes in E can have drastic changes in $\langle A \rangle$ (see $E \simeq 12.4$ kPa, Fig. 3D). An overview of all investigated experimental conditions is

Preprints (www.preprints.org) | NOT PEER-REVIEWED | Posted: 7 June 2022 doi:10.20944/preprints202206.0095.v1

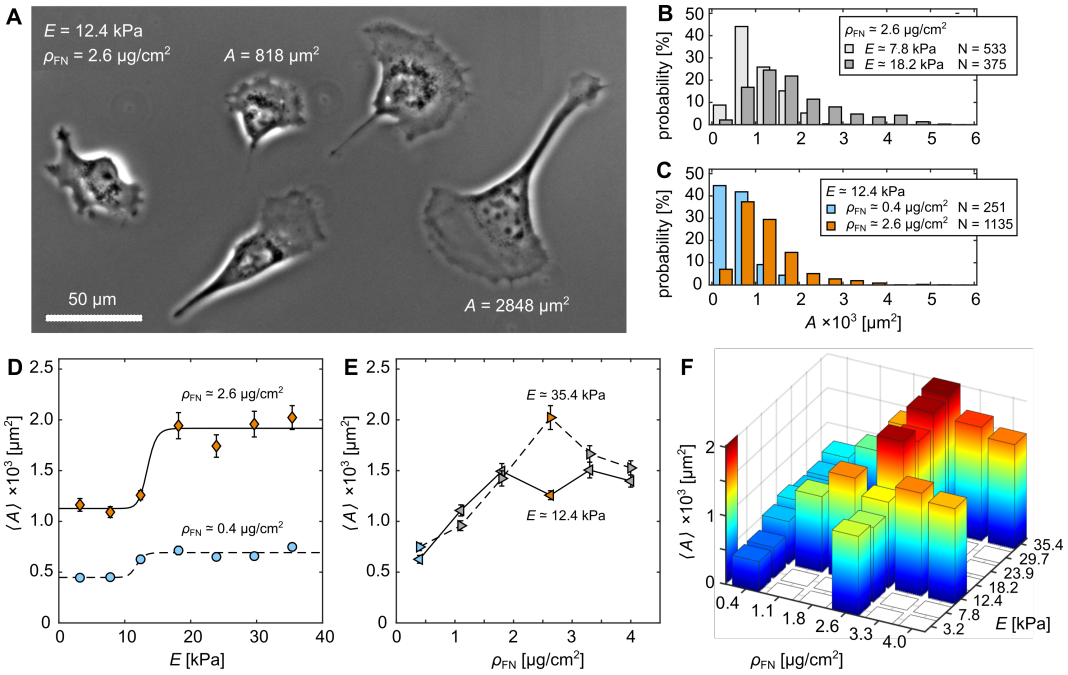

Figure 3. Cell area dependence on functionalized rigid hydrogels. **A** Phase contrast image of C2C12 cells on substrate rigidity $E \simeq 12.4$ kPa and fibronectin coated density $\rho_{\mathrm{FN}} \simeq 2.6\ \mu\mathrm{g/cm}^2$. **B** Probability histograms of projected cell areas A for two substrate rigidities E at constant fibronectin density $\rho_{\mathrm{FN}} \simeq 2.6\ \mu\mathrm{g/cm}^2$. **C** Probability histograms of A for two different ρ_{FN} at constant $E \simeq 12.4$ kPa. **D** Mean projected cell areas, $\langle A \rangle$ as a function of E for two different ρ_{FN}. The dashed lines are fits of the hill-equation (Eq. 16). **E** $\langle A \rangle$ as a function of ρ_{FN} at $E \simeq 12.4$ kPa (left pointed triangles) and $E \simeq 35.4$ kPa (right pointed triangles). **D-E** Another visualization of the distributions is illustrated in Fig. S2. The color scheme used in **C-E** relates to cells that are cultured on substrates functionalized with $\rho_{\mathrm{FN}} \simeq 0.4\ \mu\mathrm{g/cm}^2$ (blue) and $\rho_{\mathrm{FN}} \simeq 2.6\ \mu\mathrm{g/cm}^2$ (orange). **F** Two-dimensional histogram of $\langle A \rangle$ as a function of E and ρ_{FN}. The errorbars indicate the standard error (see Materials and Methods).

shown in Fig. 3F.

An alternative explanation can be drawn from the skewed normal distributions (Figs. 3C-D). The degree of skewness, i.e. right tail of distribution, strongly influences the resulting $\langle A \rangle$. Cells cultured on hydrogels with larger E and larger ρ_{FN} show stronger skewness. In order to take this effect into account and probe the effect of the statistical outcome, the area distributions were fitted to a mixture of two normal probability density functions (MN-pdf) (see Eq. 13 and Figs. 4A-B, red solid lines). This leads to two splitted $\langle A \rangle$ for each distribution, a lower and a higher one that represent the position of the first, main peak and shallower second peak for larger cells (see Figs. 4A-B, blue dashed lines). In doing so, the degree of skewness loses its strong influence on the mean $\langle A \rangle$ calculated for the entire distribution. Figure 4C shows the two splitted $\langle A \rangle$ as a function of ρ_{FN} at the fixed substrate rigidities $E \simeq 12.4$ kPa and $E \simeq 35.4$ kPa. Following the approach of Zemel et. al (2010) for quantifying the cell area as a function of the substrate rigidity parameterised by the aspect ratio of cells[16], the data were fitted with the Lorentz-like function as

$$\mathcal{L}(\rho_{\mathrm{FN}}) = \langle A \rangle = \frac{x_1 \rho_{\mathrm{FN}}}{x_2(\rho_{\mathrm{FN}} - x_3)^2 + 1} + x_4, \tag{17}$$

where x_i are fitting parameter. The black solid and dashed lines are the respective fits (Fig. 4C). A clear correlation between $\langle A \rangle$ and ρ_{FN} is observed, although the degree of skewness, i.e. relative amount of larger cells, significantly varies between different substrate conditions. A maximum for all four curves is found at about 2 $\mu\mathrm{g/cm}^2$ to 3 $\mu\mathrm{g/cm}^2$. There

Preprints (www.preprints.org) | NOT PEER-REVIEWED | Posted: 7 June 2022 doi:10.20944/preprints202206.0095.v1

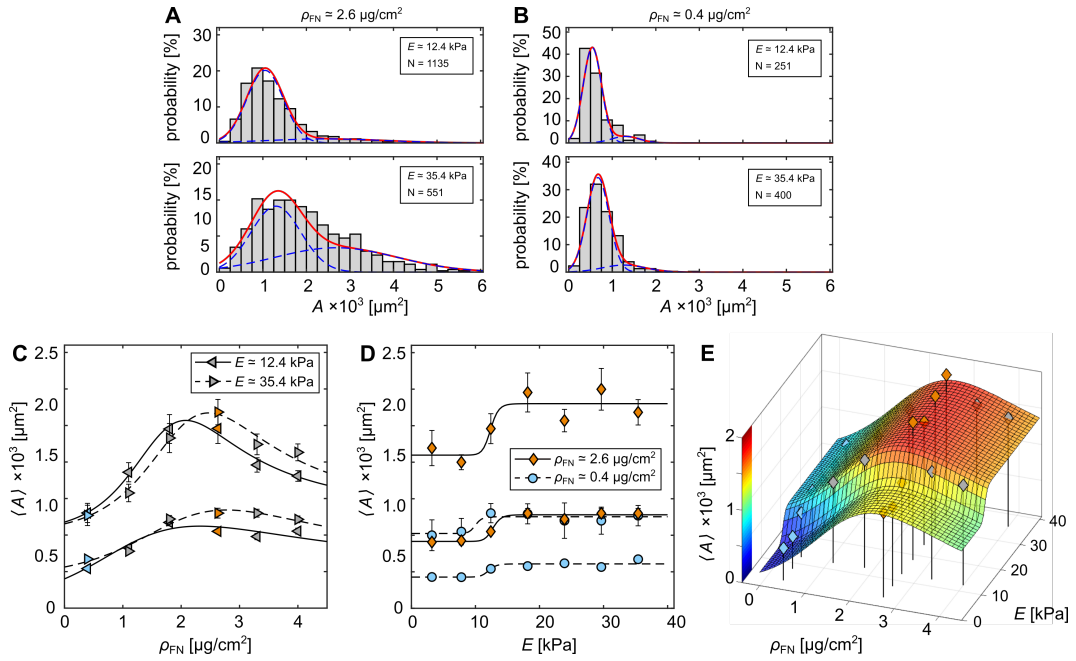

Figure 4. Cross-talk between hydrogel rigidity and fibronectin density. **A-B** Example of area distributions fitted by MN-pdf (see Eq. 13). Red line are MN-pdf, and blue lines are the two individual normal distributions. Shown are distributions for $\rho_{\mathrm{FN}} \simeq 2.6$ (**A**) and $\rho_{\mathrm{FN}} \simeq 0.4$ (**B**) for $E \simeq 12.4$ kPa and $E \simeq 35.4$ kPa. **C** Lower and higher means $\langle A \rangle$ of the obtained MN-pdfs as a function of ρ_{FN} at $E \simeq 12.4$ kPa (left pointed triangles) and $E \simeq 35.4$ kPa (right pointed triangles). Solid and dashed lines are fits of the Lorentz equation (Eq. 17) for the two Young's moduli. The data correspond to the data shown in Fig. 3E. **D** Lower and higher means $\langle A \rangle$ of the obtained MN-pdfs as a function of E for $\rho_{\mathrm{FN}} \simeq 0.4$ μg/cm^2 (blue circles) and $\rho_{\mathrm{FN}} \simeq 2.6$ μg/cm^2 (orange diamonds) and in correspondence with Hill fits (Eq. 16). The errorbars in **C** and **D** indicate the respective standard errors (see Eq. 15). **E** Two-dimensional relationship of $\langle A \rangle$ as a function of E and ρ_{FN} corresponding to the data in **C** and **D**. The fit is calculated by considering Eq. 18.

is no slightly lower kink at $\rho_{\mathrm{FN}} \simeq 2.6$ μg/cm^2 visible (Fig. 3E). Figure 4D illustrates $\langle A \rangle$ as a function of E following the same approach. The Hill fits lead also to comparable characteristic half levels at about $E_{1/2} \simeq 12$ kPa and $E_{1/2} \simeq 13$ kPa, as obtained in Fig. 3D. Consequently, the kink found at $\rho_{\mathrm{FN}} \simeq 2.6$ μg/cm^2 can be explained by the lower number of cells that lead to the secondary normal distribution of larger cells. Thus, this can be interpreted as an optimization of cellular mechanosensing to the ECM, as most of the cells have similar sizes, caused by the significantly lower degree of skewness (see also Figs. 4A-B). Taking advantage of the more representative statistical analysis, all data were fitted to equation

$$\langle A \rangle = \frac{\mathcal{H}(E) + \mathcal{L}(\rho_{\mathrm{FN}})}{2}, \tag{18}$$

where $\mathcal{H}$ and $\mathcal{L}$ are correspond the Hill equation (Eq. 16) and Lorentz-like equation (Eq. 17). Figure 4D shows the three-dimensional relation between the E, ρ_{FN}, and $\langle A \rangle$. The latter is back-scaled by the fraction, p between the two split $\langle A \rangle$ (see Eq. 13).

Cytoskeletal actin response to substrate properties

Next, we investigated the F-actin formation in C2C12 muscle cells. After 24 hours incubation, the actin and nucleus of cells were stained and observed with confocal microscopy (see Material and Methods). Figure 5A illustrates a snapshot of such an observation at two different fibronectin surface-densities, $\rho_{\mathrm{FN}} \simeq 0.4$ μg/cm^2 and $\rho_{\mathrm{FN}} \simeq 2.6$ μg/cm^2, with $E \simeq 12.4$ kPa. The two center panels correspond to sections of priorly processed images by AQuA (dashed rectangles left and right panel). The alignment angle of the actin

Preprints (www.preprints.org) | NOT PEER-REVIEWED | Posted: 7 June 2022 doi:10.20944/preprints202206.0095.v1

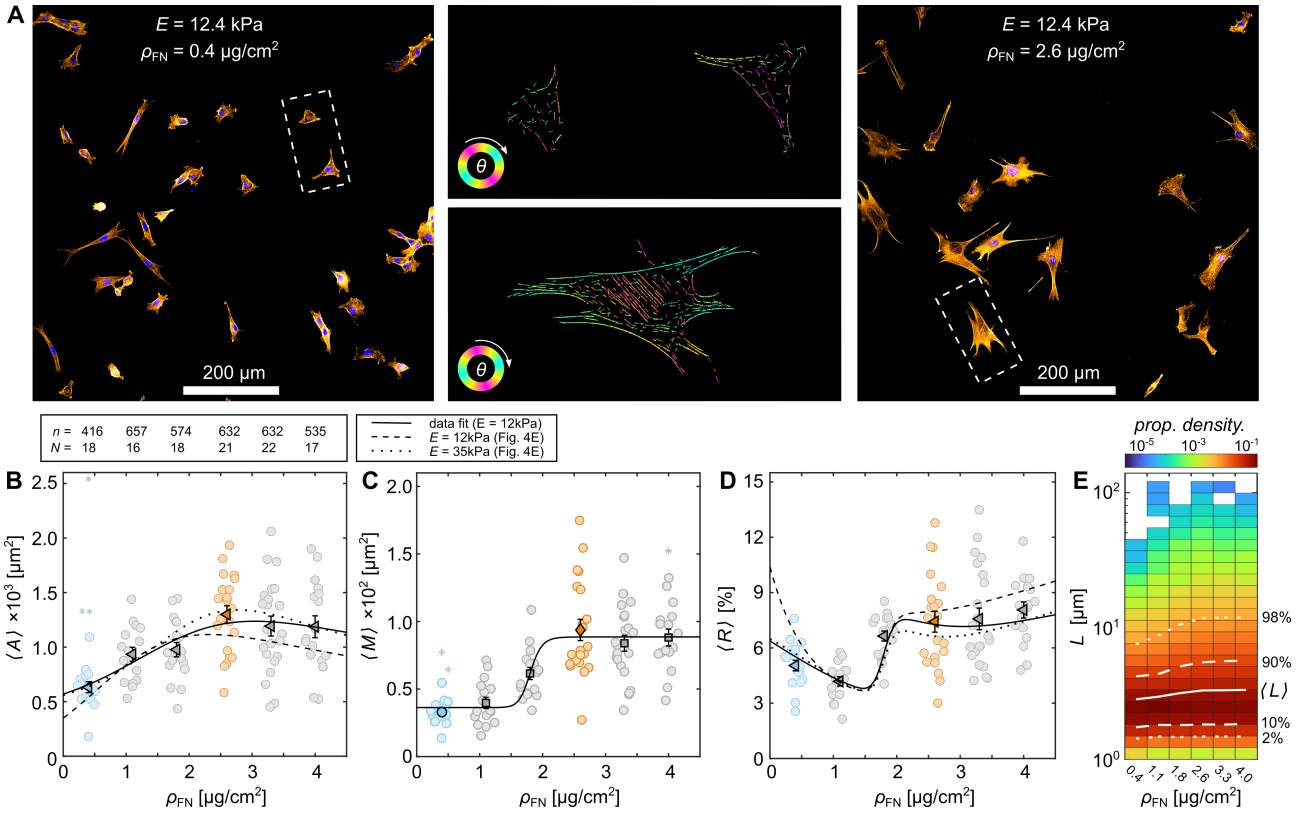

Figure 5. Actin cytoskeleton formation dependence on fibronectin density. **A** Actin and cell nuclei labeled confocal images of C2C12 cells on $E \simeq 12.4$ kPa hydrogels coated with $\rho_{FN} \simeq 0.4$ µg/cm^2 (left panel) and $\rho_{FN} \simeq 2.6$ µg/cm^2 (right panel). Two exemplarily sections of priorly processed images by AQuA (middle panel) are illustrated from these two ρ_{FN} (dashed selection, left and right panel). **B-D** Statistical analysis of mean projected cell areas $\langle A \rangle$, mean amount of actin $\langle M \rangle$, and fraction of actin amount to cell area $\langle R \rangle$ of the 5×5 tiled images. The respective number of images N and sum of the containing cell, i.e. nuclei, n is written on top of **B**. Each bright colored round data point is calculated from one 5×5 tiled image, and the mean and standard error of those are shown by the darker colored data points. Substrates functionalized with $\rho_{FN} \simeq 0.4$ µg/cm^2 and $\rho_{FN} \simeq 2.6$ µg/cm^2 are highlighted in blue and orange. Asterisks depict outliers (see Materials and Methods). **E** Probability density of the actin fibre length L. Percentiles of 2%, 10%, 90%, and 98% are marked by white dashed and dotted lines. $\langle L \rangle$ is marked as white solid line.

filaments were visualized as a function of the color scheme (see Materials and Methods). No preferred alignment angle hast been observed, as homogeneous substrates without micro-groves were prepared [5]. The statistical analysis of the average projected cell areas $\langle A \rangle$ and average amount of actin per C2C12 cell $\langle M \rangle$ revealed a similar Hill-function-like dependence to ρ_{FN} at fixed hydrogel rigidity $E \simeq 12.4$ kPa (Fig. 5B and C). $\langle A \rangle$ and $\langle M \rangle$ increase up to $\rho_{FN} \simeq 2.6$ µg/cm^2 and saturate thereafter. Contrarily to the results shown in Fig. 3E, here no kink at $\rho_{FN} \simeq 2.6$ µg/cm^2 is observed, as the statistical approach differs. Here, a large field of view (about 1×1 mm^2) is automatically analyzed without taking the single cell into account. By scaling the integrated sum of cell area by the counted number of nuclei, we obtained an averaged $\langle A \rangle_N$ (Fig. 3B, bright data points). This was used to calculate the mean $\langle A \rangle$. Again $\mathcal{L}(\rho_{FN})$ fits the data well (Fig. 5B, solid line). For comparison, the fit of $\mathcal{L}$ from Fig. 4C (lower solid line) is plotted as dashed line, which also represents the data well, as cells cultured on rigid hydrogels with $\rho_{FN} \simeq 2.6$ µg/cm^2 and $E \simeq 12.4$ kPa exhibit a more pronounced normal distribution that is less skewed. The same statistical approach is used for $\langle M \rangle$ (Fig. 5C). Contrarily, $\langle M \rangle$ follows a Hill-like distribution, as shown by the fit of $\mathcal{H}(\rho_{FN})$ (Fig. 5C) with a characteristic half level at about

Preprints (www.preprints.org) | NOT PEER-REVIEWED | Posted: 7 June 2022 doi:10.20944/preprints202206.0095.v1

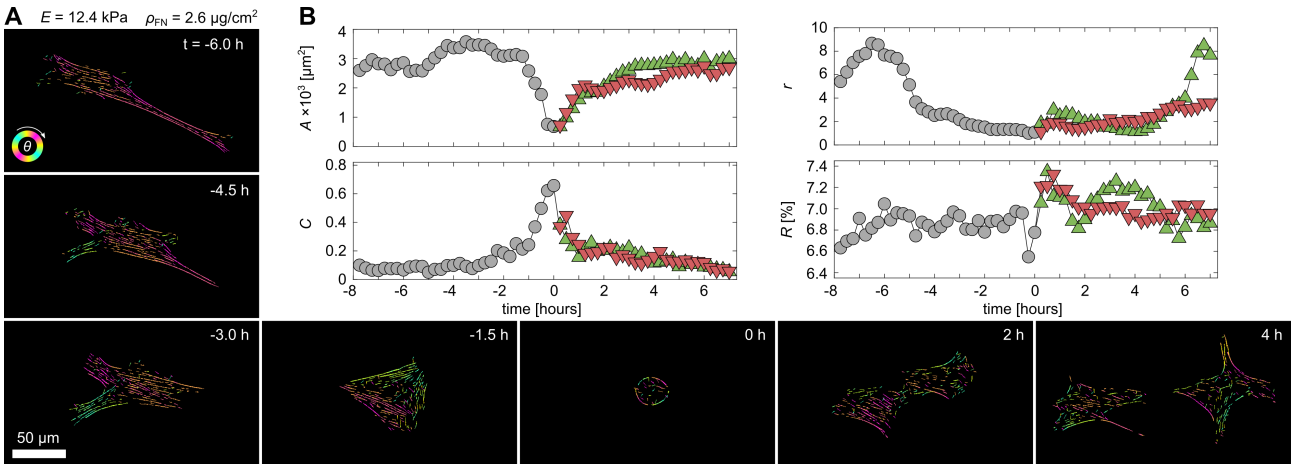

Figure 6. Proliferation dynamic of a single myocyte on a rigid hydrogel. **A** Snapshots of a C2C12 muscle cell that undergoes proliferation at about $t = 0$ min on a $E \simeq 12.4$ kPa hydrogel coated with $\rho_{\mathrm{FN}} \simeq 2.6$ µg/cm^2. The images are processed by AQuA. **B** Temporal tracking of the projected cell area A, the circularity C, aspect ratio r, and fraction of actin amount to cell area R during 15 hours of cell migration and proliferation. The mother and two daughter cells are distinguished by grey circles, green upward- and red downward-pointing triangles.

$\rho_{\mathrm{FN}} \simeq 1.8$ µg/cm^2. The fraction of actin amount to cell area $\langle R \rangle$ (see Eq. 6) shows two distinct plateaus (Fig. 4D). Both fits (solid and dashed line) derived from $\langle A \rangle$ and $\langle M \rangle$ are in good agreement with the data (triangles). A plateau at about $\langle R \rangle_{\mathrm{max}} \simeq 7.5\%$ is observed from about 2 µg/cm^2. Considering that the thickness of actin bundles is not directly taken into account in AQuA, this indicates an almost two times denser actin cytoskeleton when ρ_{FN} is at least 2.6 µg/cm^2. This is also visible at the difference of actin fibre length L, as shown as probability density distribution in Figure 5E. The average actin fibre length $\langle L \rangle$ is shown as solid white stripe for all conditions, indicating a proportional relation to $\langle A \rangle$.

Monitoring the actin fibre formation dynamics of single myocytes before and after proliferation shows similar results (Fig. 6A). Here, on a hydrogel with $\rho_{\mathrm{FN}} \simeq 2.6$ and $E \simeq 12.4$ kPa, the area of cells A decreases only temporally before and after proliferation from a large adhered cell, e.g. $t = -6$ h, to a round barely adhered cell just before cell devision at $t = 0$ h, and back to large adherent daughter cells after a few hours. Figure 6B shows the projected area A, the circularity C, aspect ratio r_A, and fraction of actin amount to cell area R. Once the mother cell (grey round points) divides into two daughter cells (green upward- and red downward-pointing triangles) all cell parameters recover within a few hours. The shape of the cell, e.g. r, changed rather dynamically during the observation time, while A and C showed rather stable plateaus before and after cell devision. However, those plateaus are marked by the symmetric decrease and increase in A and C, since the proliferation of single cells in culture is marked by the actin-depolarization and thus rounding of the projected cell shape ($t \simeq 0$, Fig. 6B), similarly as monitored for cells that dynamically adjust to a softer ECM[3]. Contrarily, R does not change much during proliferation and seems therefore a stable cell specific parameter. For this particular cell R is about 7%.

In the next section, we investigated proliferation dynamics, e.g. temporal change in A, on rigid hydrogels with un-labeled cells to gain information on different substrate properties, as the fluorescence expression rate in life-imaging observations is rather inequally distributed among cells and might lead to phenotype-biased statistical results even in fluorescence-activated cell sorted (FACS) cultures (not shown).

Preprints (www.preprints.org) | NOT PEER-REVIEWED | Posted: 7 June 2022 doi:10.20944/preprints202206.0095.v1

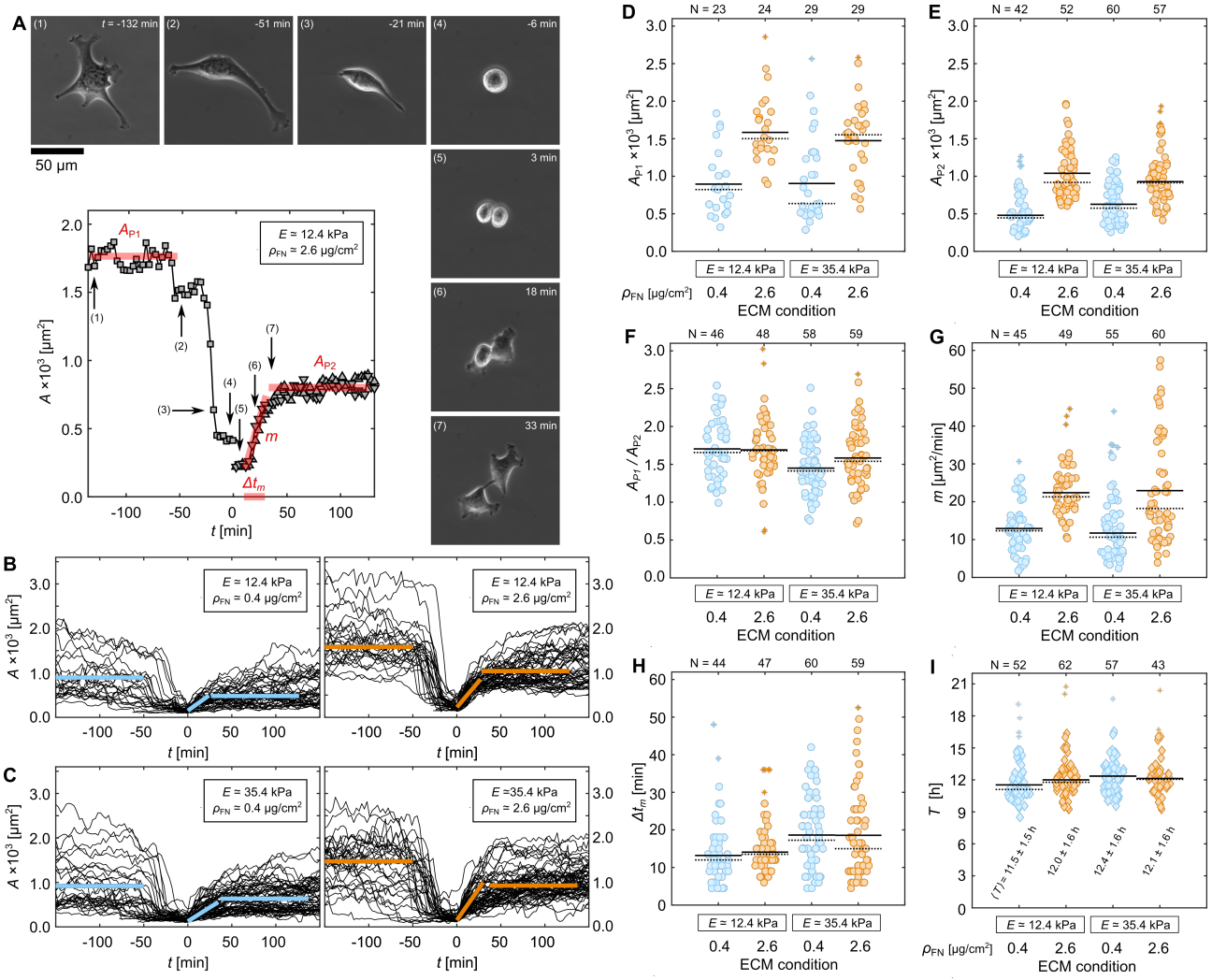

Figure 7. Proliferation dynamics depend on the ECM. **A** Example of a C2C12 muscle cell on a $E \simeq 12.4$ kPa hydrogel coated with $\rho_{FN} \simeq 2.6$ µg/cm^2 and the corresponding projected cell area A as a function of time. **B** The time evolution of the A of cells cultured on $E \simeq 12.4$ kPa hydrogels coated with either 0.4 µg/cm^2 (left panel) or 2.6 µg/cm^2 (right panel). **C** The time evolution of the A of cells cultured on $E \simeq 35.4$ kPa hydrogels coated with either 0.4 µg/cm^2 (left panel) or 2.6 µg/cm^2 (right panel). **D-H** Statistical analysis of the cell trajectories (**B** and **C**). Shown are the following extracted parameter: area plateau of the mother cells A_{P1}, area plateau of the daughter cells A_{P2}, area ratio of mother to daughter cells A_{P2}/A_{P2}, initial spreading rate m after cell division, and duration of spreading Δt_m as a function of E and ρ_{FN}. The parameters are exemplarily highlighted in red solid lines in **A**. **I** Cell cycle duration T, i.e. duration between two successive cell devisions. Means and medians are illustrated by solid and dotted lines. Number of data points are written on top of the plots by N excluding the outliers that are highlighted by asterisks. Substrates functionalized with $\rho_{FN} \simeq 0.4$ µg/cm^2 and $\rho_{FN} \simeq 2.6$ µg/cm^2 are highlighted in blue and orange.

Quantification of proliferation dynamics

Investigating temporal-resolved cellular dynamics offers a closer look to study the dynamic responses to different substrate conditions. As it is unclear at what state in the cell cycle each cell is during observation, we focus on the proliferation dynamics, and therefore enable comparability of the morphological changes. For single cell observations the proliferation is clearly visible due to depolimerization of the actin cytoskeleton before the mother cell divides into two daughter cells (t = [-1 : 0] hours, Fig. 6). Further, in unlabelled cells this rapid decline can be observed in the change of cell area. A typical

Preprints (www.preprints.org) | NOT PEER-REVIEWED | Posted: 7 June 2022 doi:10.20944/preprints202206.0095.v1

change in A is also observed after the cell devision as a rapid increase and subsequent initial plateau in A (Fig. 7A). For statistical comparison, the different states were quantified by the area plateau A_{P1} before the proliferation, the slope m and duration Δt_m, that describes the linear cell spreading after the proliferation, and the following area plateau A_{P2} (red lines, Fig. 7A). A_{P1} was chosen to be at least 50 min before the proliferation, as some cells exhibit a step-like decline in A followed by a sudden exponential decrease (see (2) and (3), Fig. 7A). Both plateaus, A_{P1} and A_{P2}, were defined about, but not longer than, 100 min. Figures 7B and C show the projected area of all cells cultured on $E \simeq 12.4$ and $E \simeq 35.4$ kPa rigid hydrogels with two differently functionalized, low ($\rho_{\mathrm{FN}} \simeq 0.4$ µg/cm^2) and high ($\rho_{\mathrm{FN}} \simeq 2.6$ µg/cm^2), fibronectin concentrations. While a general substrate-conditional trend is visible, large variations among cells are observed within one condition, as seen by the quantified state-parameter (Figs. 7A-H). Both plateaus, A_{P1} and A_{P2}, show hydrogel-rigidity independent mean values that vary only by the difference in ρ_{FN} (see for comparison Figs. 3E, 4C, and 5B). However, the fraction A_{P1}/A_{P2} illustrates a more stable recovery when cells are cultured on $E \simeq 12.4$ kPa rigid hydrogels, as A_{P1}/A_{P2} is larger and independent of ρ_{FN}. The differences in area fraction are mainly governed by the different cell spreading dynamics after proliferation. While m is again substrate-rigidity independent, Δt_m depends on the rigidity but surprisingly does not exhibit an influence on the amount of fibronectin. That means that cells cultured on stiffer hydrogels spread longer until reaching the plateau, but not faster, as m is comparable for both substrate rigidities. Further, an increased variability among cells in m and Δt_m is observed for the stiffer hydrogels with higher fibronectin condition ($E \simeq 35.4$ kPa; $\rho_{\mathrm{FN}} \simeq 2.6$ µg/cm^2). The area plateaus, however, did not show such an increased variability. To see how differences in the spreading dynamics affect the cell cycle duration T, independent time-lapse experiments were performed where only the cell division duration between two successive cell devisions was extracted. Although cells substantially behave differently on different substrate conditions (Figs. 7A-H), no significant difference in T is observed. A mean cell cycle duration $\langle T \rangle$ of about 12 hours was observed (Figs. 7I). As all cells were cultured 24 hours prior to observation, we can estimate that the measured individual cell cycle duration corresponds to at least the third generation of cells.

4. Conclusions

In this study, we utilized L-DOPA functionalized rigid hydrogels to explore the morphological response of single C2C12 cells to different compositions of substrate rigidity and fibronectin coating density. The projected area of cells clearly correlates to the substrate rigidity independent to the fibronectin density when the elastic modulus is about 12 kPa. Statistically, cells exhibited larger projected areas when the fibronectin density was higher. Additionally, cells that were cultured on hydrogels with different fibronectin densities exhibited the largest projected areas at $\rho_{\mathrm{FN}} \simeq 2.6$ µg/cm^2. This optimum is explained by the increase of the second subpopulation of cells that consists of especially large cells, as confirmed by an independent statistical analysis of the same data using a combination of two normal distributions rather than a single distribution analysis. This combination of normal distributions enables a more precise estimation of the statistical distribution of cell areas. This finding was independently confirmed by actin stained cells on 12 kPa rigid hydrogels. Again the same optimal fibronectin density was identified at 2.6 µg/cm^2. Further, the quantified amount of actin showed a step-like function that could be quantified by the empirical Hill equation with a characteristic half level at about 1.8 µg/cm^2. Beyond this critical fibronectin density, cells increased the amount of actin, which also correlates with the actin to cell area ratio that was determined to be about 7.5 %. Lower fibronectin densities lead to a minimum actin to cell area ratio down to 4 % close to 1 µg/cm^2.

Moreover, we investigated the proliferation dynamics for four different substrate conditions by comparing combinations between two elastic moduli (12.4 kPa and 35.4 kPa) and two fibronectin coating densities (0.4 µg/cm^2 and 2.6 µg/cm^2). We parameter-

 doi:10.20944/preprints202206.0095.v1

ized the phase contrast recorded cells and compared the four different conditions of the extra cellular matrix. While the results of the area plateaus before and after proliferation related to the obtained results of the morphological response of single C2C12 cells, we have identified interesting differences in the cell spreading dynamics just after the proliferation. The spreading speed correlates to the elastic modulus of the hydrogel, while the duration of spreading correlates with the fibronectin density until reaching the area plateau. Contrarily, no difference in the cell cycle duration was observed. All conditions led to an average cell cycle duration of about 12 hours. Although we did not observe any statistically significant differences in the cycle duration, those findings may also be in part explainable by the deformation of the nucleus due to an increased actomyosin tension, as previously reported[39]. The correlation of cell spreading and substrate elasticity was shown before[40] and explained through the substrate stress relaxation that is mediated through integrin adhesions and actomyosin-based contractility, and the increased nuclear translocation of YAP driven by stress relaxation[41]. YAP (Yes-associated protein) is a transcriptional regulator that requires Rho activity to regulate mechanical properties of the ECM and cell geometry[42]. In mesenchymal stem cells, the percentage of cells with YAP in the nucleus increases linearly with increases in the elastic modulus, reaching a plateau at 10 kPa[43]. Considering a comparable YAP dependence in C2C12 cells, our findings suggest a potential link between the cell spreading duration after proliferation with the content of YAP in the nucleus (Fig. 7H), while the cell spreading speed is solely regulated by the amount of matrix proteins in the ECM (Fig. 7G). The exact mechanism of how the actin cytoskeleton impacts YAP in the context of mechanotransduction is still unknown[44], however, YAP activation is known to increase cardiomyocyte proliferation and regeneration[45,46], which relates to our findings.

While both, the cell area and the actin amount, are good markers to identify the optimal fibronectin coating density, the presented results suggest that the amount of actin is the favourable cell characteristic to study the influence of extracellular matrix proteins. Another advantage is the faster and more accurate automated data analysis that was not reliably implementable for the phase contrast recorded cells. In this study, those images were manually segmented, as automated segmentation methods could not reach the quality that is necessary for a comprehensive statistical analysis. Furthermore, the use of L-DOPA turned out to be much more reliable to functionalize matrix proteins to rigid hydrogels. Most studies use Sulfo-Sanpah to functionalize hydrogels[3,39,47,48], however, it is rather unreliable, and thus, difficult to reproduce comparable results. L-DOPA, on the other hand, has many advantages, such as a simpler protocol, no UV radiation necessary, RT-storage, relatively low in price, and artefact free during images.

In this study, we focused on the mechano-regulative feedback of single myocytes to different extracelluar matrix properties. The extracellular environment is critical to maintain cellular integrity and functionality of more sensitive myocyte cultures, such as embryonic and inducible pluripotent stem-cells [20], as well as primary cultures of neonatal animals[2]. The latter is especially important to study the effect of the life-threatening induction of alternans, where the mechanoregulation, tissue arrangement and synchonization dynamics play an essential role[2,49,50]. Thus, the methodology and results presented in this manuscript provide a fundamental platform to investigate more complex myocyte dynamics.

Author Contributions: Conceptualization, M.H.; formal analysis, JB, JE, SE, and MH; data curation, J.B., J.E., and M.H.; data segmentation, J.B. and M.H.; writing—original draft preparation, J.B., J.E., and M.H.; writing—review and editing, J.B., J.E., S.E., and M.H.; supervision, M.H.; All authors have read and agreed to the published version of the manuscript.

Funding: This research received no external funding.

Institutional Review Board Statement: Not applicable

Data Availability Statement: The data that support the findings of this study are available on request from the corresponding authors.

Acknowledgments: We thank Katja Abing and Aleksander Drinic for their initial experiments and Melanie Noack for the technical support. We thank Dr. Joachim Spatz and Cornelia Miksch for the provision of the AFM at the Max Planck Institute for Intelligent Systems, Stuttgart, Germany. We thank Dr. Arnd Heyer and Dr. Ingrid Weiss for the fruitful discussions.

Conflicts of Interest: The authors declare no conflict of interest.

Abbreviations

The following abbreviations are used in this manuscript:

FN	fibronectin
RT	room temperature
ECM	extracellular matrix
AQuA	Actin Quantification Analysis
DMEM	Dulbecco's modified Eagle's medium
eLoG	elongated Laplace of Gaussian

References

1. Urbanczyk, M.; Layland, S.L.; Schenke-Layland, K. The Role of Extracellular Matrix in Biomechanics and Its Impact on Bioengineering of Cells and 3D Tissues. *Matrix Biology* **2020**, *85–86*, 1–14. doi:10.1016/j.matbio.2019.11.005.
2. Hörning, M.; Kidoaki, S.; Kawano, T.; Yoshikawa, K. Rigidity Matching between Cells and the Extracellular Matrix Leads to the Stabilization of Cardiac Conduction. *Biophysical Journal* **2012**, *102*, 379–387. doi:10.1016/j.bpj.2011.12.018.
3. Hörning, M.; Nakahata, M.; Linke, P.; Yamamoto, A.; Veschgini, M.; Kaufmann, S.; Takashima, Y.; Harada, A.; Tanaka, M. Dynamic Mechano-Regulation of Myoblast Cells on Supramolecular Hydrogels Cross-Linked by Reversible Host-Guest Interactions. *Scientific Reports* **2017**, *7*, 7660. doi:10.1038/s41598-017-07934-x.
4. Yin, L.; Bien, H.; Entcheva, E. Scaffold Topography Alters Intracellular Calcium Dynamics in Cultured Cardiomyocyte Networks. *American Journal of Physiology-Heart and Circulatory Physiology* **2004**, *287*, H1276–H1285. doi:10.1152/ajpheart.01120.2003.
5. Erben, A.; Hörning, M.; Hartmann, B.; Becke, T.; Eisler, S.A.; Southan, A.; Cranz, S.; Hayden, O.; Kneidinger, N.; Königshoff, M.; et al. Precision 3D-Printed Cell Scaffolds Mimicking Native Tissue Composition and Mechanics. *Advanced Healthcare Materials* **2020**, *n/a*, 2000918. doi:10.1002/adhm.202000918.
6. Harburger, D.S.; Calderwood, D.A. Integrin Signalling at a Glance. *Journal of Cell Science* **2009**, *122*, 159–163. doi:10.1242/jcs.018093.
7. Takagi, Y.; Homsher, E.E.; Goldman, Y.E.; Shuman, H. Force Generation in Single Conventional Actomyosin Complexes under High Dynamic Load. *Biophysical Journal* **2006**, *90*, 1295–1307. doi:10.1529/biophysj.105.068429.
8. Lo, C.W. Role of Gap Junctions in Cardiac Conduction and Development. *Circulation Research* **2000**, *87*, 346–348. doi:10.1161/01.RES.87.5.346.
9. Miura, K.; Siegert, F. Light Affects cAMP Signaling and Cell Movement Activity in Dictyostelium Discoideum. *Proceedings of the National Academy of Sciences* **2000**, *97*, 2111–2116. doi:10.1073/pnas.040554497.
10. Ali-Murthy, Z.; Kornberg, T.B. Bicoid Gradient Formation and Function in the Drosophila Pre-Syncytial Blastoderm. *eLife* **2016**, *5*, e13222. doi:10.7554/eLife.13222.
11. Zhang, Z.; Zwick, S.; Loew, E.; Grimley, J.S.; Ramanathan, S. Mouse Embryo Geometry Drives Formation of Robust Signaling Gradients through Receptor Localization. *Nature Communications* **2019**, *10*, 4516. doi:10.1038/s41467-019-12533-7.
12. Capron, A.; Chatfield, S.; Provart, N.; Berleth, T. Embryogenesis: Pattern Formation from a Single Cell. *The Arabidopsis Book / American Society of Plant Biologists* **2009**, *7*, e0126. doi:10.1199/tab.0126.
13. Engler, A.J.; Sen, S.; Sweeney, H.L.; Discher, D.E. Matrix Elasticity Directs Stem Cell Lineage Specification. *Cell* **2006**, *126*, 677–689. doi:10.1016/j.cell.2006.06.044.
14. Engler, A.J.; Griffin, M.A.; Sen, S.; Bönnemann, C.G.; Sweeney, H.L.; Discher, D.E. Myotubes Differentiate Optimally on Substrates with Tissue-like Stiffness: Pathological Implications for Soft or Stiff Microenvironments. *J Cell Biol* **2004**, *166*, 877–887. doi:10.1083/jcb.200405004.
15. Engler, A.J.; Carag-Krieger, C.; Johnson, C.P.; Raab, M.; Tang, H.Y.; Speicher, D.W.; Sanger, J.W.; Sanger, J.M.; Discher, D.E. Embryonic Cardiomyocytes Beat Best on a Matrix with Heart-like Elasticity: Scar-like Rigidity Inhibits Beating. *Journal of Cell Science* **2008**, *121*, 3794–3802. doi:10.1242/jcs.029678.
16. Zemel, A.; Rehfeldt, F.; Brown, A.E.X.; Discher, D.E.; Safran, S.A. Optimal Matrix Rigidity for Stress Fiber Polarization in Stem Cells. *Nature Physics* **2010**, *6*, 468–473. doi:10.1038/nphys1613.
17. Engler, A.; Bacakova, L.; Newman, C.; Hategan, A.; Griffin, M.; Discher, D. Substrate Compliance versus Ligand Density in Cell on Gel Responses. *Biophysical Journal* **2004**, *86*, 617–628. doi:10.1016/S0006-3495(04)74140-5.

18. Schreiber, C.; Amiri, B.; Heyn, J.C.J.; Rädler, J.O.; Falcke, M. On the Adhesion–Velocity Relation and Length Adaptation of Motile Cells on Stepped Fibronectin Lanes. *Proceedings of the National Academy of Sciences* **2021**, *118*. doi:10.1073/pnas.2009959118.
19. Yoshikawa, H.Y.; Rossetti, F.F.; Kaufmann, S.; Kaindl, T.; Madsen, J.; Engel, U.; Lewis, A.L.; Armes, S.P.; Tanaka, M. Quantitative Evaluation of Mechanosensing of Cells on Dynamically Tunable Hydrogels. *Journal of the American Chemical Society* **2011**, *133*, 1367–1374. doi:10.1021/ja1060615.
20. Li, J.; Zhang, L.; Yu, L.; Minami, I.; Miyagawa, S.; Hörning, M.; Dong, J.; Qiao, J.; Qu, X.; Hua, Y.; et al. Circulating Re-Entrant Waves Promote Maturation of hiPSC-derived Cardiomyocytes in Self-Organized Tissue Ring. *Communications Biology* **2020**, *3*, 1–12. doi:10.1038/s42003-020-0853-0.
21. Trappmann, B.; Gautrot, J.E.; Connelly, J.T.; Strange, D.G.T.; Li, Y.; Oyen, M.L.; Stuart, M.A.C.; Boehm, H.; Li, B.; Vogel, V.; et al. Extracellular-Matrix Tethering Regulates Stem-Cell Fate. *Nature Materials* **2012**, *11*, 642–649. doi:10.1038/nmat3339.
22. Kern, W.; Puotinen, D. Cleaning Solutions Based on Hydrogen Peroxide for Use in Silicon Semiconductor Technology. *RCA Rev.* **1970**, *31*, 187–206.
23. Kidoaki, S.; Matsuda, T. Microelastic Gradient Gelatinous Gels to Induce Cellular Mechanotaxis. *Journal of Biotechnology* **2008**, *133*, 225–230. doi:10.1016/j.jbiotec.2007.08.015.
24. Buxboim, A.; Rajagopal, K.; Brown, A.E.X.; Discher, D.E. How Deeply Cells Feel: Methods for Thin Gels. *Journal of Physics: Condensed Matter* **2010**, *22*, 194116. doi:10.1088/0953-8984/22/19/194116.
25. Butt, H.J.; Cappella, B.; Kappl, M. Force Measurements with the Atomic Force Microscope: Technique, Interpretation and Applications. *Surface Science Reports* **2005**, *59*, 1–152. doi:10.1016/j.surfrep.2005.08.003.
26. Sneddon, I.N. The Relation between Load and Penetration in the Axisymmetric Boussinesq Problem for a Punch of Arbitrary Profile. *International Journal of Engineering Science* **1965**, *3*, 47–57. doi:10.1016/0020-7225(65)90019-4.
27. Domke, J.; Radmacher, M. Measuring the Elastic Properties of Thin Polymer Films with the Atomic Force Microscope. *Langmuir* **1998**, *14*, 3320–3325. doi:10.1021/la9713006.
28. Lin, D.C.; Dimitriadis, E.K.; Horkay, F. Robust Strategies for Automated AFM Force Curve Analysis—I. Non-adhesive Indentation of Soft, Inhomogeneous Materials. *Journal of Biomechanical Engineering* **2006**, *129*, 430–440. doi:10.1115/1.2720924.
29. Wouters, O.Y.; Ploeger, D.T.; van Putten, S.M.; Bank, R.A. 3,4-Dihydroxy-L-Phenylalanine as a Novel Covalent Linker of Extracellular Matrix Proteins to Polyacrylamide Hydrogels with a Tunable Stiffness. *Tissue Engineering Part C: Methods* **2016**, *22*, 91–101. doi:10.1089/ten.tec.2015.0312.
30. García, A.J.; Vega, M.D.; Boettiger, D. Modulation of Cell Proliferation and Differentiation through Substrate-dependent Changes in Fibronectin Conformation. *Molecular Biology of the Cell* **1999**, *10*, 785–798.
31. Inoue, S.; Frank, V.; Hörning, M.; Kaufmann, S.; Yoshikawa, H.Y.; Madsen, J.P.; Lewis, A.L.; Armes, S.P.; Tanaka, M. Live Cell Tracking of Symmetry Break in Actin Cytoskeleton Triggered by Abrupt Changes in Micromechanical Environments. *Biomaterials Science* **2015**, *3*, 1539–1544. doi:10.1039/C5BM00205B.
32. Otsu, N. A Threshold Selection Method from Gray-Level Histograms. *IEEE Transactions on Systems, Man, and Cybernetics* **1979**, *9*, 62–66. doi:10.1109/TSMC.1979.4310076.
33. Finney, D.J. On the Distribution of a Variate Whose Logarithm Is Normally Distributed. *Supplement to the Journal of the Royal Statistical Society* **1941**, *7*, 155–161. doi:10.2307/2983663.
34. Matson, J.P.; Cook, J.G. Cell Cycle Proliferation Decisions: The Impact of Single Cell Analyses. *The FEBS journal* **2017**, *284*, 362–375. doi:10.1111/febs.13898.
35. Lira, L.M.; Martins, K.A.; de Torresi, S.I.C. Structural Parameters of Polyacrylamide Hydrogels Obtained by the Equilibrium Swelling Theory. *European Polymer Journal* **2009**, *45*, 1232–1238. doi:10.1016/j.eurpolymj.2008.12.022.
36. Oyen, M.L. Mechanical Characterisation of Hydrogel Materials. *International Materials Reviews* **2014**, *59*, 44–59. doi:10.1179/1743280413Y.0000
37. Righetti, P.G.; Brost, B.C.W.; Snyder, R.S. On the Limiting Pore Size of Hydrophilic Gels for Electrophoresis and Isoelectric Focussing. *Journal of Biochemical and Biophysical Methods* **1981**, *4*, 347–363. doi:10.1016/0165-022X(81)90075-0.
38. Bian, W.; Bursac, N. Engineered Skeletal Muscle Tissue Networks with Controllable Architecture. *Biomaterials* **2009**, *30*, 1401–1412. doi:10.1016/j.biomaterials.2008.11.015.
39. Lovett, D.B.; Shekhar, N.; Nickerson, J.A.; Roux, K.J.; Lele, T.P. Modulation of Nuclear Shape by Substrate Rigidity. *Cellular and molecular bioengineering* **2013**, *6*, 230–238. doi:10.1007/s12195-013-0270-2.
40. Gong, Z.; Szczesny, S.E.; Caliari, S.R.; Charrier, E.E.; Chaudhuri, O.; Cao, X.; Lin, Y.; Mauck, R.L.; Janmey, P.A.; Burdick, J.A.; et al. Matching Material and Cellular Timescales Maximizes Cell Spreading on Viscoelastic Substrates. *Proceedings of the National Academy of Sciences* **2018**, *115*, E2686–E2695. doi:10.1073/pnas.1716620115.
41. Chaudhuri, O.; Gu, L.; Darnell, M.; Klumpers, D.; Bencherif, S.A.; Weaver, J.C.; Huebsch, N.; Mooney, D.J. Substrate Stress Relaxation Regulates Cell Spreading. *Nature Communications* **2015**, *6*, 6365. doi:10.1038/ncomms7365.
42. Dupont, S.; Morsut, L.; Aragona, M.; Enzo, E.; Giulitti, S.; Cordenonsi, M.; Zanconato, F.; Le Digabel, J.; Forcato, M.; Bicciato, S.; et al. Role of YAP/TAZ in Mechanotransduction. *Nature* **2011**, *474*, 179–183. doi:10.1038/nature10137.
43. Yamazaki, M.; Kidoaki, S.; Fujie, H.; Miyoshi, H. Designing Elastic Modulus of Cell Culture Substrate to Regulate YAP and RUNX2 Localization for Controlling Differentiation of Human Mesenchymal Stem Cells. *Analytical Sciences* **2021**, *37*, 447–453. doi:10.2116/analsci.20SCP02.
44. Panciera, T.; Azzolin, L.; Cordenonsi, M.; Piccolo, S. Mechanobiology of YAP and TAZ in Physiology and Disease. *Nature Reviews Molecular Cell Biology* **2017**, *18*, 758–770. doi:10.1038/nrm.2017.87.

 doi:10.20944/preprints202206.0095.v1

45. Morikawa, Y.; Zhang, M.; Heallen, T.; Leach, J.; Tao, G.; Xiao, Y.; Bai, Y.; Li, W.; Willerson, J.T.; Martin, J.F. Actin Cytoskeletal Remodeling with Protrusion Formation Is Essential for Heart Regeneration in Hippo-deficient Mice. *Science signaling* **2015**, *8*, ra41. doi:10.1126/scisignal.2005781.
46. Xin, M.; Kim, Y.; Sutherland, L.B.; Murakami, M.; Qi, X.; McAnally, J.; Porrello, E.R.; Mahmoud, A.I.; Tan, W.; Shelton, J.M.; et al. Hippo Pathway Effector Yap Promotes Cardiac Regeneration. *Proceedings of the National Academy of Sciences of the United States of America* **2013**, *110*, 13839–13844. doi:10.1073/pnas.1313192110.
47. Aratyn-Schaus, Y.; Oakes, P.W.; Stricker, J.; Winter, S.P.; Gardel, M.L. Preparation of Complaint Matrices for Quantifying Cellular Contraction. *Journal of Visualized Experiments: JoVE* **2010**. doi:10.3791/2173.
48. Tse, J.R.; Engler, A.J. Preparation of Hydrogel Substrates with Tunable Mechanical Properties. *Current Protocols in Cell Biology* **2010**, *Chapter 10*, Unit 10.16. doi:10.1002/0471143030.cb1016s47.
49. Hörning, M.; Blanchard, F.; Isomura, A.; Yoshikawa, K. Dynamics of Spatiotemporal Line Defects and Chaos Control in Complex Excitable Systems. *Scientific Reports* **2017**, *7*, 7757. doi:10.1038/s41598-017-08011-z.
50. Loppini, A.; Erhardt, J.; Fenton, F.H.; Filippi, S.; Hörning, M.; Gizzi, A. Optical Ultrastructure of Large Mammalian Hearts Recovers Discordant Alternans by In Silico Data Assimilation. *Frontiers in Network Physiology* **2022**, *2*.

Preprints (www.preprints.org) | NOT PEER-REVIEWED | Posted: 7 June 2022 doi:10.20944/preprints202206.0095.v1

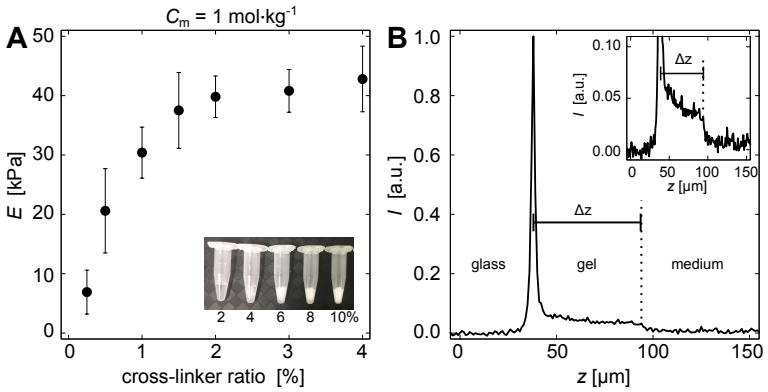

Figure 8. FIGS1: Property assessment of the poly-acrylamide hydrogels. **A** Mechanical property assessment of the poly-acrylamide hydrogels by the variation of the cross-linker ratio with a fixed total monomer concentration $C_m = 1$ mol·kg^{-1}. The inset depicts an image of poly-acrylamide hydrogels with different cross-linker ratios. Cross-linker ratios of 4% and higher lead to non-transparent hydrogels. **B** illustrates an example of the auto-fluorescence signal without a second peak (gel to medium) of a hydrogel with C_m = 1.0 mol·kg^{-}1 ($E = 12$ kPa). The inlet shows the shallow plateau that was used to estimate the gel height.

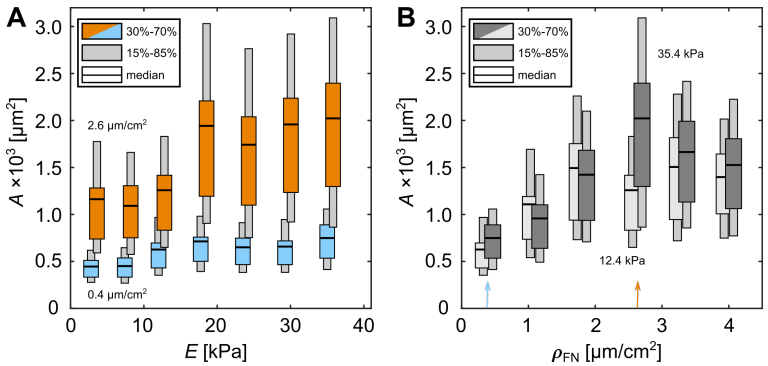

Figure 9. FIGS2: Cell area dependence on functionalized rigid hydrogels. **A** Projected cell areas, $\langle A \rangle$ as a function of E for $\rho_{\mathrm{FN}} \simeq 0.4$ µg/cm^2 (blue) and $\rho_{\mathrm{FN}} \simeq 2.6$ µg/cm^2 (orange). **B** $\langle A \rangle$ as a function of ρ_{FN} at $E \simeq 12.4$ kPa (bright grey) and $E \simeq 35.4$ kPa (dark grey). Shown are the median and percentiles of the cell area distributions (see Fig. 3**D-E**, main manuscript).